Journal of Materials Chemistry C

Anomalous thermal transport behavior in graphene-like carbon nitride (C3N)

Journal:	*Journal of Materials Chemistry C*
Manuscript ID	TC-ART-06-2022-002425.R1
Article Type:	Paper
Date Submitted by the Author:	25-Jul-2022
Complete List of Authors:	Qin, Guangzhao; Hunan University, State Key Laboratory of Advanced Design and Manufacturing for Vehicle Body lin, jianzhou; Hunan University, State Key Laboratory of Advanced Design and Manufacturing for Vehicle Body Wang, Huimin; Xiangtan University, Hunan Key Laboratory for Micro-Nano Energy Materials & Device and School of Physics and Optoelectronics Hu, Jianjun; University of South Carolina, ; Guizhou University, Qin, Zhenzhen; Zhengzhou University Hu, Ming; University of South Carolina, Mechanical Engineering

Anomalous thermal transport behavior in graphene-like carbon nitride (C_3N)

Guangzhao Qin,[1,5] Jianzhou Lin,[1] Huimin Wang,[2] Jianjun Hu,[3] Zhenzhen Qin,[4*] and Ming Hu[5*]

[1]*State Key Laboratory of Advanced Design and Manufacturing for Vehicle Body, College of Mechanical and Vehicle Engineering, Hunan University, Changsha 410082, P. R. China*

[2]*Hunan Key Laboratory for Micro-Nano Energy Materials & Device and School of Physics and Optoelectronics, Xiangtan University, Xiangtan 411105, Hunan, China*

[3]*Department of Computer Science and Engineering, University of South Carolina, Columbia, SC 29208, USA*

[4]*School of Physics and Microelectronics, Zhengzhou University, Zhengzhou 450001, China*

[5]*Department of Mechanical Engineering, University of South Carolina, Columbia, SC 29208, USA*

[*] Author to whom all correspondence should be addressed. E-Mail: Z.Q. <qzz@zzu.edu.cn>, M.H. <hu@sc.edu>

ABSTRACT

The graphene's success created a new era in materials science, especially for two-dimensional (2D) materials. Two-dimensional single-crystal carbon nitride (C_3N) whose controlled large-scale synthesis is the first and only crystalline, hole-free, single-layer carbon nitride has recently attracted tremendous interest in thermal transport. Here, we perform a comparative study of thermal transport between monolayer C_3N and the parent graphene, and focused on the effect of temperature and strain on thermal conductivity (κ) of C_3N, by solving the phonon Boltzmann transport equation (BTE) based on first-principles calculations. The κ of C_3N shows an anomalous temperature dependence, and κ of C_3N at high temperatures is larger than the expected value following the common trend of $\kappa \sim 1/T$. Moreover, the κ of C_3N is found in surprise to be enlarged by applying bilateral tensile strain, despite its similar planar honeycomb structure as graphene. The underlying mechanism is revealed by providing direct evidence for the interaction between lone-pair N-*s* electrons and bonding electrons from C atoms in C_3N based on the analysis of orbital-projected electronic structures and electron localization function (ELF). Our research not only conducted a comprehensive study on the thermal transport in graphene-like C_3N, but also revealed the physical origin of its anomalous properties, which will also have significant implications on the future nanoscale thermal transport.

Keywords: carbon nitride, lone-pair electrons, thermal conductivity

1. INTRODUCTION

Since the recent developments in 2004, the research field of graphene has developed rapidly and prompted an unprecedented surge of activity and demonstration of new physical phenomena with novel applications[1,2], such as nanoelectronics, energy storage and conversion, medicine, catalysis, sensors, *etc*. Graphene has lots of excellent properties such as the surprisingly large room-temperature electron mobility, high strength and flexibility, and record high thermal conductivity[3–6]. However, attempts to utilize graphene for practical applications are faced with some limitations, especially the poor on-off current ratio (I_{ON}/I_{OFF}< 100) in graphene-based devices due to the gapless nature of graphene[7]. Thus, the substitutions of carbon (C) atom in graphene with heteroatoms were stimulated for the extension of graphene family to other 2D layered crystalline materials[8]. Among these, monolayer hexagonal boron nitride (*h*-BN) with a wide band gap (~5.0-6.0 eV) offers an alternative solution beyond the gapless graphene, which establishes the key role of 2D nitrides in advancing the development of next generation nano-electronics[9]. To benefit from carbon-based nanomaterials at the same time, partially substituting C atoms in graphene with N is a plausible approach to the formation of graphene-like 2D carbon nitrides. In the past years, different N/C ratios have been realized[10–12]. For example, 2D crystalline layered C_3N_4 and C_2N-*h*2D are semiconductors with direct bandgaps of 2.76 and 1.96 eV, respectively, with potential applications in nanoelectronics, photo-catalysis, solar power generation, *etc*. However, large number of holes exist in the crystalline structures due to the large N/C ratios. Recently, Yang *et al*.[13] reported the controllable large-scale (up to hundreds of micrometer) synthesis of 2D single crystalline carbon nitride (C_3N) sheet, which is the first and the only crystalline, hole-free, single-layer carbon nitride, showing graphene-like morphology [Fig. 1(a)].

Monolayer C_3N possesses the graphene-like planar honeycomb structure with a homogeneous distribution of C and N atoms, both of which show the D_{6h}-symmetry[14]. Despite various 2D carbon-based materials, C_3N is the only one possessing indirect bandgap, which is 0.39 eV as verified both experimentally and theoretically and can be tuned to cover the entire visible range[13]. This new material has ultra high stiffness[15], excellent electronic, magnetic[13,16] and gas adsorption properties[17,18] , etc. These excellent properties facilitate its practical applications in various fields such as field-effect transistors[19], lithium-ion batteries[20], CO_2 collection and separation[21], thermoelectric[22] and energy storage materials[23]. Considering almost all the novel applications of C_3N in nanoelectronics are inevitably involved with heat dissipation, the thermal transport properties are of great interest for developing high performance C_3N-based devices in terms of efficient thermal management.

Efficient regulation of heat transfer plays a key role in the high-performance thermal management of nanotechnologies. The heat conduction in semiconductors is mainly carried out by phonon transport[1,24,25]. Therefore, the fundamental understanding of phonon transport is of great significance for the effective control of heat flow, and it is a thermophysical problem that has great practical significance related to energy technology, such as electrical cooling, thermoelectric technology, phase change storage,[1,26]thermal devices (diodes, transistors, logic gates),[27] *etc*. In the past few decades, lots of studies have focused on the effective regulation of heat transport by nanostructuring[28–30]. In addition, non-Fourier phenomena have been studied for thermal conductivity, such as phonon weak coupling[31,32] and Graded thermal conductivity[33]. Besides, pores are introduced into the physicochemical treatment (hydrogenation, oxidation, *etc*)[34]. In addition, effective thermal modulation can also be achieved by external electric/magnetic field[35] and strain engineering[36–38]. Due to the robust reliability and strong flexibility, strain engineering has become one of the most promising and effective ways to achieve continuously adjustable heat transport. Moreover, the actual case of many systems and devices typically contain residual strain after fabrication[39]. Therefore, the study of strain engineering on the regulation of thermal conductivity has a very important practical significance. However, previous studies have mainly focused on how to adjust thermal conductivity through mechanical strain, and there is still a lot of unclear understanding of the essential origin of its regulatory effects[36,38,40–43]. These in-depth understanding benefits more effective and accurate thermal conductivity regulation, which would have a far-reaching guiding role. Thus, the modulation of the thermal transport properties of monolayer C_3N by mechanical strain could be practically meaningful, and the origin of the underlying mechanism would deepen our understanding of phonon transport in 2D materials and have great impact on future research in materials design with targeted thermal transport properties.

In this paper, by solving the phonon Boltzmann transport equation (BTE) based on first-principles calculations, we perform a comparative study of phonon transport between monolayer C_3N and graphene. Besides the anomalous temperature dependence of κ of C_3N, it is very intriguing to find that the κ of C_3N is more than one order of magnitude lower than graphene, considering the similar structures and the only difference of substituting 1/4 C with N atoms in C_3N compared to graphene. By deeply analyzing the orbital projected electronic structure, we establish a microscopic picture of the lone-pair electrons driving strong phonon anharmonicity. We show that nonlinear restoring forces arise from the interactions between lone-pair electrons around N atoms and bonding electrons from adjacent atoms (C), leading to strong phonon anharmonicity and low κ. Furthermore, the κ of C_3N is unexpectedly enlarged by applying bilateral tensile

strain despite the planar honeycomb structure of C_3N (similar to graphene, with no buckling or puckering), which is in sharp contrast to the strain induced κ reduction in graphene. The opposite response of κ to mechanical strain between C_3N and graphene further supports the established microscopic picture of the lone-pair electrons driving strong phonon anharmonicity.

2. METHODS

All the first-principles calculations are performed in the framework of density functional theory (DFT) using the projector augmented wave (PAW) method[44] as implemented in the Vienna *ab initio* simulation package (VASP)[45]. The Perdew-Burke-Ernzerhof (PBE) of generalized gradient approximation (GGA) revised for solids (PBEsol)[46] is chosen as the exchange-correlation functional[47]. The kinetic energy cutoff of wave functions is set as 1000 eV and a Monkhorst-Pack[48] *k*-mesh of 31 × 31 × 1 is used to sample the Brillouin Zone(BZ) with the energy convergence threshold of 10^{-6} eV, where the k is the electronic wavevector spanned by the reciprocal lattice vectors. A large enough vacuum spacing of 20 Å is used along the *out-of-plane* direction based on the convergence test. The applied biaxial strain is defined as $(l - l_0)/l_0$, where l is the lattice constant under strains and l_0 corresponds to the original value with no strain applied. All geometries are fully optimized based on the primitive cell containing 8 atoms [6 C and 2 N as shown in Fig. 1(a)] to get the stable configuration with globally minimized energy, until the maximal Hellmann-Feynman force is smaller than 10^{-8} eV/Å. For the consistent calculations of interatomic force constants (IFCs) using the finite displacement difference method, 3 × 3 × 1 supercell containing 72 atoms is constructed and the Monkhorst-Pack *k*-mesh of 2 × 2 × 1 is used to sample the BZ, which can accurately describe the system based on the convergence test[49,50]. The space group symmetry properties are used to reduce the computational cost and the numerical noise of the forces[51]. The translational and rotational invariance of IFCs are enforced using the Lagrange multiplier method[52,53]. The Born effective charges (Z^*) and dielectric constants (ϵ) are obtained based on the density functional perturbation theory (DFPT), which are added to the dynamical matrix as a correction to take long-range electrostatic interaction into account. Based on kinetic theory, κ can be expressed as[54]

$$\kappa_\alpha = \sum_{qp} C_V(\vec{q}, p) v_\alpha(\vec{q}, p)^2 \tau(\vec{q}, p) \ , \tag{2}$$

where C_V is the volumetric specific heat capacity of phonon following the Bose-Einstein statistics, $\vec{v}_\alpha(\vec{q},p)$ is the α (= *x, y, z*) component of group velocity of phonon mode with wave vector $\vec{q}$ and polarization p, and τ is the relaxation time (phonon lifetime). The κ is obtained by iteratively solving the phonon BTE with the

ShengBTE package, which is equivalent to the solution of relaxation time approximation (RTA) if the iteration stops at the first step[53,55]. The convergence test of κ with respect to the cutoff distance and Q-grid are fully conducted[56], based on which the cutoff distance is chosen as 7.36 Å (13th nearest neighbors) for the 3rd IFCs calculations and the Q-grid is chosen as 50 × 50 × 1 for the κ calculations. The κ of graphene is calculated to be 3094.98 W/mK by using the iterative method. The good agreement with previous results confirms the reliability of our calculations[1].

3. RESULT AND DISCUSSION

Up to now, monolayer C_3N is the only crystalline, hole-free, single-layer carbon nitride[13], which shows graphene-like morphology [Fig. 1(a)]. C_3N possesses a planar honeycomb structure, different from the buckled silicene and the puckered phosphorene, with the primitive cell containing 8 atoms (6 C and 2 N), in which both C and N atoms show a D_{6h}-symmetry. The optimized lattice constant of C_3N is 4.86 Å. The C-C and C-N bond lengths in C_3N are calculated to be slightly different (1.40326 and 1.40288 Å, respectively) and show obvious isotropy. Based on the optimized structure, we calculate the phonon dispersions and partial density of states (pDOS) of C_3N [Fig. 1(b)]. No imaginary frequency is observed, indicating the thermodynamical stability of monolayer C_3N. The results of graphene are also plotted for comparison, which are calculated with the supercell of 2 × 2 × 1 (i.e. 8 atoms, the same as C_3N) used as the unit cell. We also plot the results of graphene with primitive cell (2 atoms) to give a hint. The flexural acoustic (FA) phonon branches (z-direction vibration) of both C_3N and graphene show the quadratic behavior, which is the typical feature of 2D materials[3] and is also observed in silicene and phosphorene[57–59]. The phonon dispersions of C_3N and graphene are highly consistent, especially for the longitudinal and transverse acoustic phonon branches. However, the FA phonon branch of C_3N is significantly softened (lower frequency and smaller group velocity) compared to graphene, which suggests possibly strong phonon anharmonicity.

Usually, the strength of the phonon anharmonicity can be quantified by the Grüneisen parameter, which characterizes the relationship between phonon frequency and crystal volume change. Thus, we further calculate the Grüneisen parameters of C_3N and graphene [Fig. 1(d)] to quantitatively assess the phonon anharmonicity. The magnitude of the Grüneisen parameters of C_3N are very large compared to graphene, especially for the FA phonon branch, confirming stronger phonon anharmonicity in C_3N. Considering the similar structures and the only difference of substituting 1/4 C with N atoms in C_3N compared to graphene, it is very intriguing to find the significantly softened FA phonon branch and strong phonon anharmonicity in C_3N. We will show later the electronic origin of the orbital driven strong phonon anharmonicity and the

anomalous large magnitude of Grüneisen parameter in C_3N. As it is known that strong phonon anharmonicity can give rise to low κ in ordered crystal structures, we would further study the thermal transport properties of C_3N.

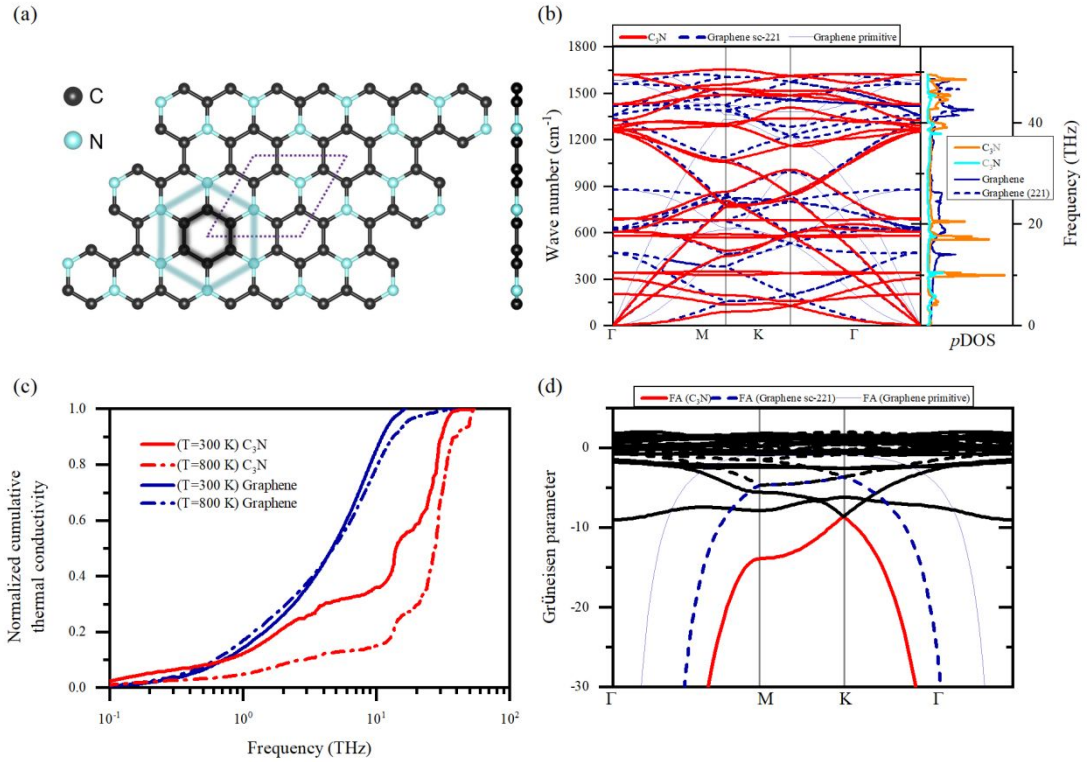

FIG. 1. (a) The top (left) and side (right) view of geometry structure of monolayer C_3N, Colored cyan and black shadow lines indicate the hexagonal structures formed by atoms C and N, respectively. Comparison of (b) phonon dispersions, partial density of states (*p*DOS), (c) the normalized cumulative κ with respect to frequency between C_3N and graphene at 300 and 800 K, and (d) Grüneisen parameters between C_3N and graphene. C_3N possesses softened FA phonon branch and the corresponding strong phonon anharmonicity.

Fig. 2(a) shows the temperature dependent κ of C_3N obtained by iteratively solving the phonon BTE together with the results from RTA method, in comparison with graphene. The room temperature κ of C_3N is 103.02 W/mK, which is more than one order of magnitude lower than that of graphene (3094.98 W/mK). So far, there are several theoretical studies on the thermal conductivity of monolayer C_3N. Table 1 summarizes the results of recent studies on C_3N, including classical non-equilibrium molecular dynamics (MD) simulation and RTA method. Note that Mortazavi[15] reported a rather high κ of C_3N (815 W/mK) based on the classical non-equilibrium MD simulations, where the optimized Tersoff and original Tersoff potentials are used to describe the C-C and C-N interatomic interactions, respectively. Considering that classical MD simulation suffers from the accuracy of the empirical potential used[57], the discrepancy of the κ between ours and Mortazavi *et al.*'s could be attributed to the different computational methods employed (first-principles *vs.* empirical potential). For example, the C-C and C-N bond lengths in C_3N are calculated to be 1.44 and 1.43 Å

in classical MD simulations, respectively[15], which also differ quite largely from the results by first-principles (1.40326 and 1.40288 Å, respectively). Besides, the differences between our calculated κ of C_3N and other first-principles results in literature can be understood from the aspects of the differences in kinetic energy cutoff, nearest neighbor, thickness, *etc*., which could affect the final thermal conductivity. For instance, for kinetic energy cutoff of wave functions, the difference between the 1000 eV used by us and the 500 eV used by Gao *et al*[60]. Besides, we have chosen a fully convergent cutoff distance of the 13th nearest neighbors, while some previous studies take smaller nearest neighbors of 5th and 8th to calculate the thermal conductivity[60–62]. Overall, it can be concluded that the κ of C_3N is one order of magnitude lower than that of graphene.

TABLE 1. Prediction of thermal conductivities for monolayer C_3N at 300 K.

Reference	Method	Lattice constant (Å)	C-C (Å)	C-N (Å)	Thickness (Å)	κ ($Wm^{-1}K^{-1}$)
This work	DFT/BTE-iterative	4.86	1.40326	1.40288	3.4	103.02
Taheri et al[63]	DFT/BTE-iterative	4.86	1.402	1.402	3.2	348
Kumar et al [62]	DFT/BTE-iterative	4.863	1.404	1.403	3.4	128
Wang et al [61]	DFT/BTE-iterative	4.86	1.403	1.404	3.2	380
Gao et al [60]	DFT/BTE-iterative		1.404	1.403	3.2	380
Peng et al [64]	DFT/BTE-iterative	4.860		1.40	3.4	482
Mortazavi[65]	MD simulation		1.44	1.43	3.2	815±20
Hong et al [66]	MD simulation				3.3	820
An et al[67]	MD simulation		1.438	1.437		535.4
Song et al[68]	MD simulation				3.2	799.87

As shown in Fig. 2(a), the κ of C_3N shows an anomalous temperature dependence, which deviates largely from the well-known $\kappa \sim 1/T$ relation, being quite different from common cases of crystalline materials[36,58,59,69–77]. In fact, the κ of C_3N has no considerable change over a large temperature range (200-800 K) due to the anomalous temperature dependence. Consequently, the κ of C_3N at high temperature is larger than the expected value following the common $\kappa \sim 1/T$ trend, which would largely benefit its applications in nano- and opto-electronics in terms of efficient heat dissipation.

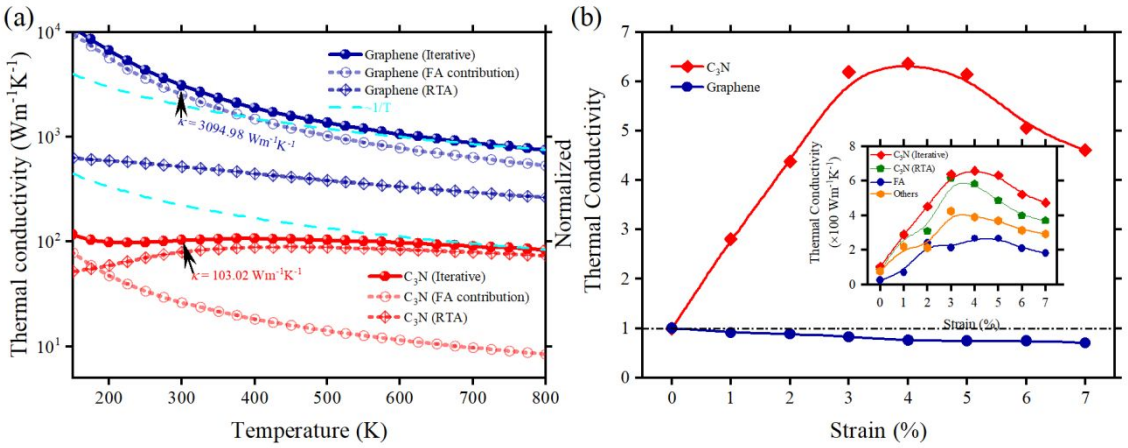

FIG. 2. (a) Comparison of the temperature dependent κ of C_3N and graphene calculated using iterative and RTA methods. The contributions from FA phonon branch and the $\kappa \sim 1/T$ relations are also plotted for comparison. (b) The unusual strain enhanced κ of C_3N, in sharp contrast to the decreasing κ of graphene.

We further investigated the effect of bilateral tensile strain on the κ of C_3N, in comparison with graphene. As shown in Fig. 2(b), the κ of graphene decreases with tensile strain, which agrees very well with previous reports[5,78,79]. In contrast, the κ of C_3N is tremendously enhanced. In previous reports on silicene, phosphene, etc., the enhancement of κ by strain engineering was considered to be specific to 2D materials with non-planar structures, and this phenomenon was attributed to the flattening of the buckled[36,43,80] and puckered[58,59,81–83] structures. As a planar 2D material without the buckled structure, it is very unusual for the anomalous positive response of κ to tensile strains in C_3N. In fact, strain engineering to increase the κ of planar 2D materials is not unique, and lin[84] et al. reported the enhancement of thermal conductivity of BC_2N with applying a small tensile strain. Therefore, it is very unusual for the anomalous positive response of κ to tensile strains in C_3N, since it has a planar honeycomb structure that is similar to graphene but different from silicene and phosphorene.

In the above discussion, the unusual properties of C_3N in terms of thermal transport can be seen, and next, in Fig. 3 and Fig. 4, we detail the mechanism underlying it. To gain insight into the mechanisms underlying the significantly lower κ of C_3N than graphene, we perform detailed mode level phonon analysis. Due to the highly consistent phonon dispersions of C_3N and graphene [Fig. 1(b)], their phonon group velocities differ from each other a little, except the FA phonon branch. The phonon group velocity of FA for C_3N is much lower compared to other phonon branches and those in graphene [Inset of Fig. 3(a)], which is due to the significant softness of FA. The relatively small phonon group velocity of FA in C_3N is partially responsible for its relatively smaller contribution to κ in C_3N (25.4%) than graphene (81.2%). Considering the similar phonon group velocity and the larger specific heat capacity of C_3N (18.94×10^5 Jm^{-3}K^{-1}) than graphene

(16.19×10^5 $Jm^{-3}K^{-1}$), the significantly lower κ of C_3N than graphene must stem from the smaller phonon life-time (larger scattering rate) based on Eq. (1), which is evidently shown in [Inset of Fig. 3(d)].

It is well-known that the scattering rate is governed by two factors: the scattering phase space and the scattering strength. As shown in [Inset of Fig. 3(c)], the scattering phase space of C_3N and graphene are consistent with each other for both the absorption and emission processes. Furthermore, we study the mode level Grüneisen parameter that quantifies the phonon anharmonicity and the scattering strength. [Inset of Fig. 3(b)] reveals that C_3N has much stronger phonon anharmonicity than graphene. The strong phonon anharmonicity in C_3N is consistent with the softened FA phonon branch [Fig. 1(b)] as analyzed above, confirming the significantly lower κ of C_3N than graphene originates from the large scattering rate [Inset of Fig. 3(d)].

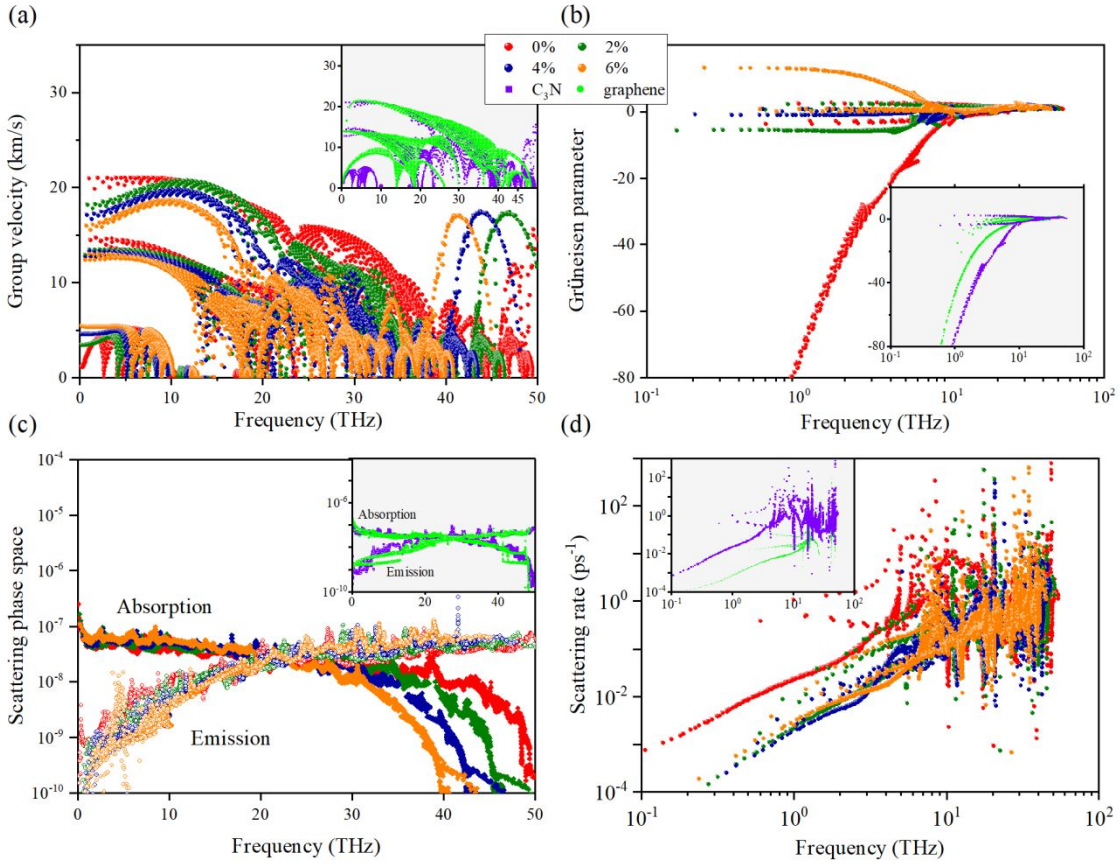

FIG. 3. Comparison of mode level (a) phonon group velocity, (b) scattering rate, (c) scattering phase space (absorption and emission process), and (d) Grüneisen parameter of C_3N between different typical strains, while comparing C_3N and graphene

As for the relatively smaller contribution from FA to κ for C_3N (25.4%) than graphene (81.2%), there are more underlying mechanisms despite the relatively small phonon group velocity of FA in C_3N caused by the significant softness of FA. The phonon scattering channels quantifying the specific scattering process among different phonon branches can provide fundamental insight into the phonon scattering process, which are ruled

by the conservation of energy and momentum[36,38,49,50,70]. The scattering rates for emission process are multiplied by 1/2 to avoid counting twice for the same process. As shown in Fig. 4(a), the scattering channels of FA phonon branch for graphene is FA+FA → TA/LA, which is governed by the so-called symmetry-based selection rule of phonon-phonon scattering. Due to the inversion symmetry of the planar structure of graphene, only the scattering channels with participation of even numbers of FA are allowed[85], leading to limited scattering rate of FA and its dominating role in phonon transport. However, it is totally different in C_3N where there exist also narrow scattering channels involving odd number of FA such as FA+O → O and FA+TA/LA → O/TA/LA in addition to the primary scattering channels of FA+FA → TA/LA [Fig. 4(b)]. Although C_3N has a planar honeycomb structure similar to graphene, the planar honeycomb structure of C_3N is not as perfectly smooth as graphene due to the difference in diameter, electronegativity, and mass of C and N atoms. The differences in diameter, electronegativity, and mass change the bond lengths and force constants, such as the subtle differences in bond lengths C-C (1.40326 Å) and C-N (1.40288 Å), reducing the symmetry of C_3N. Similar results have been also observed in previous studies. For instance, An[67] *et al.* calculated the thermal conductivity of doped graphene C_3C^{14} (C^{14} has the same coordination as the N atom in C_3N) to be 811.5 W/mK, demonstrating the effect of the difference in atomic masses in C_3N on the thermal conductivity. The scattering channels quantify the specific scattering processes between the different phonon branches, and the additional scattering channels involving odd FA reveal that the inversion symmetry in C_3N is slightly broken due to the difference in C and N diameters, masses, and electronegativities. Besides, same situation is also found in monolayer GaN[49,50]. The extra scattering channels for FA [Fig. 4(a)] in C_3N together with the relatively small phonon group velocity [Inset of Fig. 3(a)] lead to the lower contribution to κ from FA (25.4%) compared with that in graphene (81.2%).

The κ of C_3N at high temperature is larger than the expected value following the common $\kappa \sim 1/T$ trend, and the κ of C_3N has no considerable change over a large temperature range (200-800 K). To understand the underlying mechanism of the anomalous temperature dependence of κ of C_3N, we compare the frequency accumulated κ of C_3N and graphene in Fig. 1(c). For graphene, the main contribution to κ is from low-frequency acoustic phonon modes at both low and high temperatures. However, the situation in C_3N is quite different from that in graphene. High-frequency optical phonon modes contribute largely to the κ of C_3N, especially when the temperature becomes high. For instance, the contribution of the main low-frequency acoustic branch FA is consistent with the trend of $\sim 1/T$. In contrast, the contribution of high-frequency phonons to the thermal conductivity of C_3N increases with increasing temperature and at high temperatures

the optical phonon branches dominate phonon transport. For the high-frequency phonon mode, the variation is dominated by the heat capacity due to its fast increase with the thermal activation and the κ contribution increases quickly with temperature increasing, making the temperature dependence of κ deviates largely from the well-known $\kappa \sim 1/T$ relation. Hence, the relatively large contribution of high-frequency phonon modes in C_3N [Fig. 1(c)] is the direct reason for the anomalous temperature dependence of κ.

In addition to C_3N, the anomalous temperature dependence of κ was also found in monolayer gallium nitride (GaN)[49] and zinc oxide (ZnO)[86], where the high-frequency phonon modes also contribute largely to the κ. It was analyzed that[49,86] in monolayer GaN and ZnO, the large contribution from high-frequency phonon modes is due to the enhanced phonon group velocity and the relatively large phonon lifetime, which are further traced back to the strongly polarized bond due to the electronegativity and the huge phonon bandgap in the phonon dispersion due to the difference in atom mass. Here, although the electronegativity and the difference in atom mass is not large for C_3N, the group velocity of LO phonon branch is still enhanced [Inset of Fig. 3(a)] due to the LO-TO splitting caused by the polarization in C-N bond [Inset of Fig. 4(e)]. Besides, the lifetime of high-frequency phonon modes in C_3N is relatively large due to the weakened phonon-phonon scattering [Inset of Fig. 3(d)] (the scattering rate is comparable to graphene while that of low-frequency phonon modes is much larger) caused by the phonon bunching and flattening [Fig. 1(b)]. Thus, the high-frequency phonon modes contribute largely to the κ of C_3N [Fig. 1(c)], which results in the anomalous temperature dependence of κ. It is worth pointing out that, a large difference in atom mass and consequently a huge bandgap in the phonon dispersion as analyzed in previous study[49] are not necessary for the anomalous temperature dependence of κ, while phonon bunching and flattening can also have the similar effect.

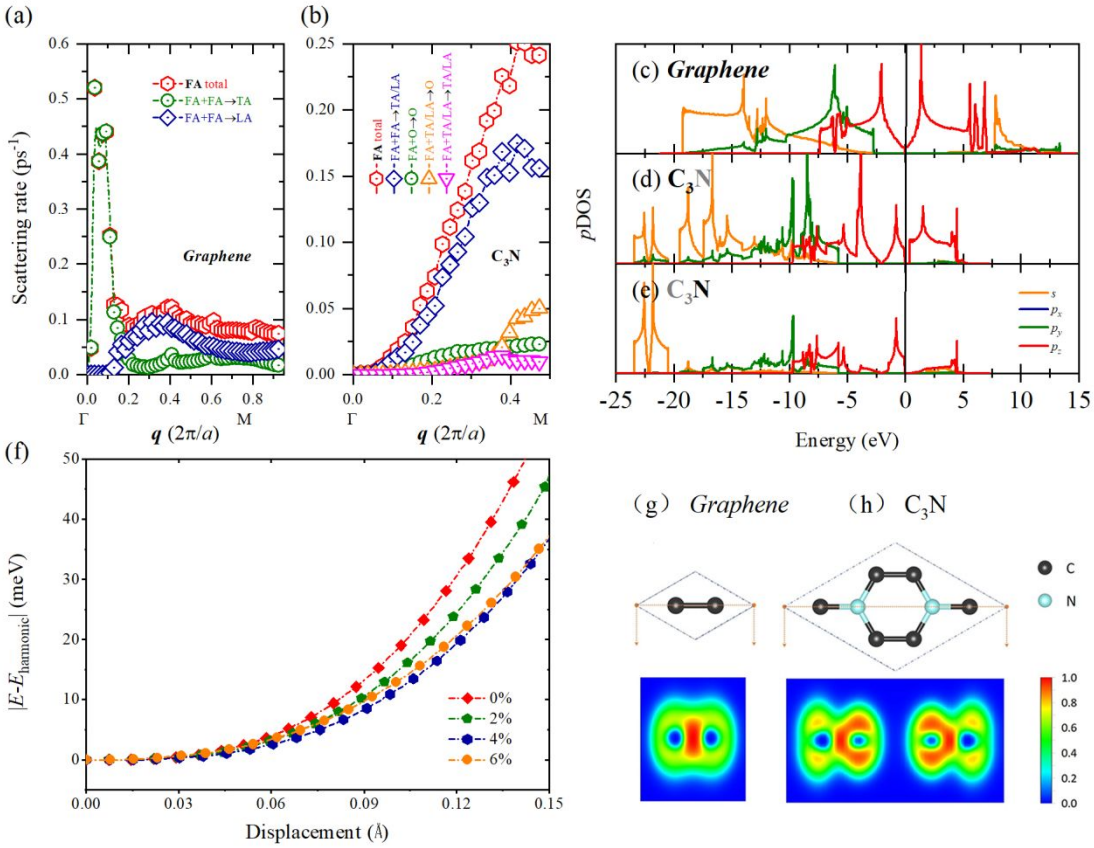

FIG. 4. Scattering channels of FA phonon modes along the Γ-M direction for (a) graphene and (b) C_3N. The *s*, p_x, p_y, and p_z orbital projected electronic density of states (*p*DOS) of (c-e) graphene and C_3N with the contributions from atoms (d) C and (e) N decoupled. (f) Energy deviation from the harmonic profile of C_3N with different typical strains applied. Inset: The displacement direction of N atom in the primitive cell. Note that the *in-plane* p_x and p_y orbitals overlap with each other. (g,h) Side view of the electron localization function (ELF) of (g) graphene and (h) C_3N. The atomic representations are top view and the ELF is taken along the orange dotted line.

As a planar 2D material without the buckled structure, it is very unusual for the anomalous positive response of κ to tensile strains in C_3N. To investigate the mechanism of enhancing the κ of C_3N with tensile strain, we further perform analysis on fundamental analysis of orbital projected electronic structures and show that the stereochemically active lone-pair electrons due to the special orbital hybridization drives the remarkable phonon anharmonicity in C_3N, as shown in Fig. S1 and Fig. 4(c), (d), and (e). With a tensile mechanical strain applied, the interaction strength would be weakened due to the increased distance, which is inferred to reduce the phonon anharmonicity and thus enlarge the κ of C_3N.

We study the contribution to κ of C_3N from different phonon branches with strain applied. As shown in the inset of Fig. 2(b), the absolute contribution to κ from FA phonon branch and all the others keep consistent with the variation trend of the total κ, and the relative contribution keeps almost the same. Detailed mode level

analysis based on Fig. 3(a, b, c, and d) reveals that the phonon group velocity and scattering phase space almost keep unchanged with strain applied, except the little decrease of group velocity. Note that due to phonon bunching of high-frequency phonon modes caused by the softened phonon dispersions, the scattering phase space of absorption process for high-frequency phonon modes decreases [Fig. 3(c)]. However, the scattering phase space of the dominating emission process for high-frequency phonon modes keeps unchanged. Thus, the largely strain enhanced κ of C_3N is primarily due to the overall weakened phonon-phonon scattering [Fig. 3(d)], which is governed by the strain weakened phonon anharmonicity as quantified by the Grüneisen parameters [Fig. 3(b)].

The κ of C_3N at high temperature is larger than the expected value following the common $\kappa \sim 1/T$ trend, and the κ of C_3N has no considerable change over a large temperature range (200-800 K). To understand the underlying mechanism of the anomalous temperature dependence of κ of C_3N, we compare the frequency accumulated κ of C_3N and graphene in Fig. 1(c). For graphene, the main contribution to κ is from low-frequency acoustic phonon modes at both low and high temperatures. However, the situation in C_3N is quite different from that in graphene. High-frequency optical phonon modes contribute largely to the κ of C_3N, especially when the temperature becomes high. For instance, the contribution of the main low-frequency acoustic branch FA is consistent with the trend of $\sim 1/T$. In contrast, the contribution of high-frequency phonons to the thermal conductivity of C_3N increases with increasing temperature and at high temperatures the optical phonon branches dominate phonon transport. For the high-frequency phonon mode, the variation is dominated by the heat capacity due to its fast increase with the thermal activation and the κ contribution increases quickly with temperature increasing, making the temperature dependence of κ deviates largely from the well-known $\kappa \sim 1/T$ relation. Hence, the relatively large contribution of high-frequency phonon modes in C_3N [Fig. 1(c)] is the direct reason for the anomalous temperature dependence of κ.

It was proposed by Petrov and Shtrum that the overlapping wave functions of lone-pair electrons with valence electrons from adjacent atoms induce nonlinear electrostatic forces upon thermal agitation, leading to increased phonon anharmonicity in the lattice and thus reducing the κ[87–93]. In graphene, the C-$s/p_x/p_y$ orbitals hybridize and contribute to the C-C σ bonds, while the C-p_z orbital comes into being the π bonds and the electronic Dirac cone[1], which are evidently shown in Fig. 4(c). The intrinsic electronic bandgap of C_3N is calculated to be 0.39 eV, which agrees perfectly with previous studies and experimental measurements[13,14]. As shown in Fig. 4(d), the orbital hybridization of C atom in C_3N are similar to graphene that the hybridized C-$s/p_x/p_y$ orbitals contribute to the σ bonds and C-p_z orbital contributes to the weakened π bonds despite the

intrinsic electronic bandgap. The situation for the orbitals is different for the N atom where the s orbital is largely (~20 eV) confined below the valence band, forming an isolated band [Fig. 4(e)]. As a result, the σ bonds linking C and N atoms are jointly contributed by the valence configuration of C-$s/p_x/p_y$ and N-$p_x/p_y/p_z$, where the s^2 electrons in the N-s^2p^3 do not participate in the bonding. Note that the doping of s^2 electrons from N atoms leads to the up-shift of Fermi level in C_3N compared to graphene [Fig. 4(d)], which opens the intrinsic bandgap above the maintained Dirac cone[94].Here, based on the above analysis and shown in Fig. 4(d, e, and h), it is clearly shown that the non-bonding lone-pair electrons arise around N atoms in C_3N due to the special orbital hybridization. The N-s electrons interact with the covalently bonding electrons of adjacent atoms (C) due to the orbital distribution in the same energy range [Fig. 4(d, e)] and wave functions overlap [Fig. 4(h)].

Additional non-linear electrostatic force among atoms is induced by the interactions when they thermally vibrate around the equilibrium positions. Consequently, a more asymmetric potential energy well would be induced, which reveals the strong phonon anharmonicity in C_3N [Fig. 1(d)] and significantly reduces the κ [Fig. 2(a)]. Thus, based on the fundamental orbital hybridizations analysis of the electronic structures, direct evidence is provided in Fig. 4(d, e, and h) for the interactions between lone-pair electrons around N atoms and bonding electrons from adjacent C atoms. Moreover, the microscopic picture is established to explain how the phonon anharmonicity arises from the view of electronic structure and leads to the low κ. Furthermore, it should be noted that there exists slight difference in the electronegativity of C and N atoms, with a difference of 0.49. Polarization of the C-N bonds is generated by the different electronegativity as evidently revealed by the electron localization function (ELF), in contrast to the nonpolarized C-C bonds [Fig. 4(g)] and (h)]. Consequently, the bonding electrons for the C-N bonds is relatively closer to N atom, which contributes positively to the stronger interaction with the non-bonding N-*s* electrons and thus leads to a stronger phonon anharmonicity.

The underlying mechanism for the anomalous strain enhanced κ of C_3N can be well understood based on the microscopic picture of the lone-pair electrons driving phonon anharmonicity as established in this work. With tensile strain applied, the separation distance between atoms becomes larger. Thus, the interaction between the lone-pair electrons around N atoms and the bonding electrons of adjacent atoms (C) are weakened. Consequently, the phonon anharmonicity is attenuated, reducing phonon-phonon scattering[95]. Based on the microscopic picture, the strain enhanced κ of C_3N is well understood. In fact, the opposite response of κ to stretching between C_3N and graphene further supports the established microscopic picture of

the lone-pair electrons driving strong phonon anharmonicity. Furthermore, it is anticipated that other systems possessing lone-pair electrons should also have a low κ and their κ can be generally enhanced by weakening the interaction strength between the lone-pair electrons and the bonding electrons of adjacent atoms, such as by increasing the bonding length with tensile strain. The possible systems possessing lone-pair electrons might be group V compounds, just name a few, *h*-BC_2N, *h*-BN, *h*-AlN, *h*-GaN, and *h*-BAs.

7. CONCLUSIONS

In summary, we have performed a comparative study of phonon thermal transport between monolayer C_3N and graphene. The κ of C_3N shows an anomalous temperature dependence, which is totally different from that for common crystalline materials and deviates largely from the well-known $\kappa \sim 1/T$ relationship. Consequently, the κ of C_3N at high temperatures is larger than the expected value that follows the general trend of $\kappa \sim 1/T$, which would be much beneficial for the applications in nano-and opto-electronics in terms of efficient heat dissipation. Moreover, it is very intriguing to find that the κ of C_3N is substantially lower than graphene, considering the similar structures and the only difference of substituting 1/4 C with N atoms in C_3N compared to graphene. The large scattering rate is responsible for the significantly low κ of C_3N, which is due to the strong phonon anharmonicity. By deeply analyzing the orbital projected electronic structure, we establish a microscopic picture of the lone-pair electrons driving strong phonon anharmonicity. Direct evidence is provided for the interactions between lone-pair electrons (N-*s*) and bonding electrons from adjacent atoms (C), which induce nonlinear electrostatic force among atoms when they thermally vibrate around the equilibrium positions, leading to the strong phonon anharmonicity and significantly low κ of C_3N. Furthermore, the κ of C_3N is unexpectedly enlarged by applying bilateral tensile strain despite the planar honeycomb structure of C_3N (similar to graphene, with no buckling or puckering), which is in sharp contrast to the strain induced κ reduction in graphene. The anomalous positive response of κ to tensile strain is attributed to the attenuated interaction between the lone-pair s electrons around N atoms and the bonding electrons of neighboring C atoms, which reduces phonon anharmonicity. The opposite response of κ to mechanical strain between C_3N and graphene further supports the established microscopic picture of the lone-pair electrons driving strong phonon anharmonicity. We propose that other systems possessing lone-pair electrons would also have low κ and the κ can be generally enhanced by weakening the interaction strength between the lone-pair electrons and the bonding electrons of adjacent atoms, such as by increasing the bonding length with tensile mechanical strain. The microscopic picture for the lone-pair electrons driving phonon anharmonicity established from the fundamental level of electronic structure deepens our

understanding of phonon transport in 2D materials and would also have great impact on future research in micro-/nano-scale thermal transport such as materials design with targeted thermal transport properties.

ACKNOWLEDGMENTS

This work is supported by the National Natural Science Foundation of China (Grant No. 52006057), the Fundamental Research Funds for the Central Universities (Grant Nos. 531119200237, and 541109010001), and the State Key Laboratory of Advanced Design and Manufacturing for Vehicle Body at Hunan University (Grant No. 52175011). This work is also supported by the Deutsche Forschungsgemeinschaft (DFG) (Project number: HU 2269/2-1). Z.Q. is supported by the National Natural Science Foundation of China (Grant No. 11847158) and the China Postdoctoral Science Foundation (2018M642776). M.H. is supported by the NSF and SC EPSCoR/IDeA Program under award number (NS-F Award Number OIA-1655740 and SC EPSCoR/IDeA Award Number 19-SA06). The numerical calculations in this paper have been done on the supercomputing system of the National Supercomputing Center in Changsha and is also supported by RWTH Aachen University under projects of jara0168 and rwth0223.

References

1 A. A. Balandin and D. L. Nika, *Materials Today*, 2012, **15**, 266–275.
2 A. K. Geim and K. S. Novoselov, *Nature Materials*, 2007, **6**, 183–191.
3 A. H. Castro Neto, F. Guinea, N. M. R. Peres, K. S. Novoselov and A. K. Geim, *Reviews of Modern Physics*, 2009, **81**, 109–162.
4 G. Zhang and Y.-W. Zhang, *Mechanics of Materials*, 2015, **91**, 382–398.
5 F. Ma, H. B. Zheng, Y. J. Sun, D. Yang, K. W. Xu and P. K. Chu, *Applied Physics Letters*, 2012, **101**, 111904.
6 G. Barbarino, C. Melis and L. Colombo, *Phys. Rev. B*, 2015, **91**, 035416.
7 K. Kim, J.-Y. Choi, T. Kim, S.-H. Cho and H.-J. Chung, *Nature*, 2011, **479**, 338–344.
8 A. C. Ferrari, F. Bonaccorso, V. Fal'Ko, K. S. Novoselov, S. Roche, P. Bøggild, S. Borini, F. H. Koppens, V. Palermo and N. Pugno, *Nanoscale*, 2015, **7**, 4598–4810.
9 J. Wu, B. Wang, Y. Wei, R. Yang and M. Dresselhaus, *Materials Research Letters*, 2013, **1**, 200–206.
10 J. Liu, Y. Liu, N. Liu, Y. Han, X. Zhang, H. Huang, Y. Lifshitz, S.-T. Lee, J. Zhong and Z. Kang, *Science*, 2015, **347**, 970–974.
11 X. Wang, K. Maeda, A. Thomas, K. Takanabe, G. Xin, J. M. Carlsson, K. Domen and M. Antonietti, *Nature materials*, 2009, **8**, 76–80.
12 J. Mahmood, E. K. Lee, M. Jung, D. Shin, I.-Y. Jeon, S.-M. Jung, H.-J. Choi, J.-M. Seo, S.-Y. Bae and S.-D. Sohn, *Nature communications*, 2015, **6**, 1–7.
13 S. Yang, W. Li, C. Ye, G. Wang, H. Tian, C. Zhu, P. He, G. Ding, X. Xie and Y. Liu, *Advanced Materials*, 2017, **29**, 1605625.

14 J. Mahmood, E. K. Lee, M. Jung, D. Shin, H.-J. Choi, J.-M. Seo, S.-M. Jung, D. Kim, F. Li and M. S. Lah, *Proceedings of the National Academy of Sciences*, 2016, **113**, 7414–7419.

15 B. Mortazavi, *Carbon*, 2017, **118**, 25–34.

16 Z. Wu, H. Zhang, J. Lin, J. Zhao and X. Cheng, *CHEMICAL PHYSICS*, , DOI:10.1016/j.chemphys.2019.110471.

17 Z. Zhao, Y. Yong, S. Hu, C. Li and Y. Kuang, *AIP ADVANCES*, , DOI:10.1063/1.5128803.

18 A. Bafekry, M. Ghergherehchi, S. F. Shayesteh and F. M. Peeters, *CHEMICAL PHYSICS*, , DOI:10.1016/j.chemphys.2019.110442.

19 T. Zhang, H. Zeng, D. Ding and R. S. Chen, *IEEE TRANSACTIONS ON ELECTRON DEVICES*, 2019, **66**, 1087–1091.

20 W. Nong, Y. Li and C. Wang, *APPLIED SURFACE SCIENCE*, , DOI:10.1016/j.apsusc.2020.145324.

21 X. Li, T. Guo, L. Zhu, C. Ling, Q. Xue and W. Xing, *CHEMICAL ENGINEERING JOURNAL*, 2018, **338**, 92–98.

22 W. Y. Jiao, R. Hu, S. Han, Y. F. Luo, H. Yuan, M. K. Li and H. Liu, *Nanotechnology*, , DOI:10.1088/1361-6528/ac302c.

23 Z. Gao, Y. Wang, Y. Meng, B. Xie, Z. Ni and S. Xia, *CHEMICAL PHYSICS LETTERS*, , DOI:10.1016/j.cplett.2021.139015.

24 A. A. Balandin, *Nature materials*, 2011, **10**, 569–581.

25 X. Gu and R. Yang, *Annual review of heat transfer*.

26 D. G. Cahill, P. V. Braun, G. Chen, D. R. Clarke, S. Fan, K. E. Goodson, P. Keblinski, W. P. King, G. D. Mahan and A. Majumdar, *Applied physics reviews*, 2014, **1**, 011305.

27 B. Li, L. Wang and G. Casati, *Physical review letters*, 2004, **93**, 184301.

28 M. Hu, K. P. Giapis, J. V. Goicochea, X. Zhang and D. Poulikakos, *Nano letters*, 2011, **11**, 618–623.

29 C. Chiritescu, D. G. Cahill, N. Nguyen, D. Johnson, A. Bodapati, P. Keblinski and P. Zschack, *Science*, 2007, **315**, 351–353.

30 W.-L. Ong, E. S. O'Brien, P. S. Dougherty, D. W. Paley, C. F. Higgs III, A. J. McGaughey, J. A. Malen and X. Roy, *Nature materials*, 2017, **16**, 83–88.

31 潘东楷, 宗志成 and 杨诺, *Acta Phys. Sin.*, 2022, **71**, 086302–5.

32 C. Deng, Y. Huang, M. An and N. Yang, *Materials Today Physics*, 2021, **16**, 100305.

33 C. Zhang, D. Ma, M. Shang, X. Wan, J.-T. Lü, Z. Guo, B. Li and N. Yang, *Materials Today Physics*, 2022, **22**, 100605.

34 L. Yang, N. Yang and B. Li, *Nano letters*, 2014, **14**, 1734–1738.

35 G. Qin, Z. Qin, S.-Y. Yue, Q.-B. Yan and M. Hu, *Nanoscale*, 2017, **9**, 7227–7234.

36 H. Xie, T. Ouyang, É. Germaneau, G. Qin, M. Hu and H. Bao, *Physical Review B*, 2016, **93**, 075404.

37 X. Li, K. Maute, M. L. Dunn and R. Yang, *Physical Review B*, 2010, **81**, 245318.

38 H. Liu, G. Qin, Y. Lin and M. Hu, *Nano letters*, 2016, **16**, 3831–3842.

39 R. Liang, J. Wang and J. Xu, *Tsinghua Science and Technology*, 2009, **14**, 62–67.

40 S. Bhowmick and V. B. Shenoy, *The Journal of chemical physics*, 2006, **125**, 164513.

41 K. D. Parrish, A. Jain, J. M. Larkin, W. A. Saidi and A. J. McGaughey, *Physical Review B*, 2014, **90**, 235201.

42 Y. Han, G. Qin, C. Jungemann and M. Hu, *Nanotechnology*, 2016, **27**, 265706.

43 M. Hu, X. Zhang and D. Poulikakos, *Physical Review B*, 2013, **87**, 195417.
44 G. Kresse and D. Joubert, *Physical review b*, 1999, **59**, 1758.
45 G. Kresse and J. Furthmüller, *Physical review B*, 1996, **54**, 11169.
46 J. P. Perdew, A. Ruzsinszky, G. I. Csonka, O. A. Vydrov, G. E. Scuseria, L. A. Constantin, X. Zhou and K. Burke, *Physical review letters*, 2008, **100**, 136406.
47 G. Qin, Z. Qin, H. Wang and M. Hu, *Computational Materials Science*, 2018, **151**, 153–159.
48 H. J. Monkhorst and J. D. Pack, *Physical review B*, 1976, **13**, 5188.
49 G. Qin, Z. Qin, H. Wang and M. Hu, *Physical Review B*, 2017, **95**, 195416.
50 Z. Qin, G. Qin, X. Zuo, Z. Xiong and M. Hu, *Nanoscale*, 2017, **9**, 4295–4309.
51 A. Togo, F. Oba and I. Tanaka, *Physical Review B*, 2008, **78**, 134106.
52 K. Esfarjani and H. T. Stokes, *Physical Review B*, 2008, **77**, 144112.
53 W. Li, L. Lindsay, D. A. Broido, D. A. Stewart and N. Mingo, *Physical Review B*, 2012, **86**, 174307.
54 D. A. Broido, A. Ward and N. Mingo, *Physical Review B*, 2005, **72**, 014308.
55 W. Li, J. Carrete, N. A. Katcho and N. Mingo, *Computer Physics Communications*, 2014, **185**, 1747–1758.
56 G. Qin and M. Hu, *npj Computational Materials*, 2018, **4**, 1–6.
57 X. Zhang, H. Xie, M. Hu, H. Bao, S. Yue, G. Qin and G. Su, *Physical Review B*, 2014, **89**, 054310.
58 G. Qin, Q.-B. Yan, Z. Qin, S.-Y. Yue, M. Hu and G. Su, *Phys. Chem. Chem. Phys.*, 2015, **17**, 4854–4858.
59 G. Qin, X. Zhang, S.-Y. Yue, Z. Qin, H. Wang, Y. Han and M. Hu, *Physical Review B*, 2016, **94**, 165445.
60 Y. Gao, H. Wang, M. Sun, Y. Ding, L. Zhang and Q. Li, *PHYSICA E-LOW-DIMENSIONAL SYSTEMS & NANOSTRUCTURES*, 2018, **99**, 194–201.
61 H. Wang, Q. Li, H. Pan, Y. Gao and M. Sun, *JOURNAL OF APPLIED PHYSICS*, , DOI:10.1063/1.5122678.
62 S. Kumar, S. Sharma, V. Babar and U. Schwingenschlogl, *JOURNAL OF MATERIALS CHEMISTRY A*, 2017, **5**, 20407–20411.
63 A. Taheri, C. Da Silva and C. H. Amon, *JOURNAL OF APPLIED PHYSICS*, , DOI:10.1063/5.0006775.
64 B. Peng, B. Mortazavi, H. Zhang, H. Shao, K. Xu, J. Li, G. Ni, T. Rabczuk and H. Zhu, *PHYSICAL REVIEW APPLIED*, , DOI:10.1103/PhysRevApplied.10.034046.
65 B. Mortazavi, *Carbon*, 2017, **118**, 25–34.
66 Y. Hong, J. Zhang and X. C. Zeng, *NANOSCALE*, 2018, **10**, 4301–4310.
67 M. An, L. Li, S. Hu, Z. Ding, X. Yu, B. Demir, N. Yang, W. Ma and X. Zhang, *Carbon*, 2020, **162**, 202–208.
68 J. Song, Z. Xu, X. He, Y. Bai, L. Miao, C. Cai and R. Wang, *Phys. Chem. Chem. Phys.*, 2019, **21**, 12977–12985.
69 J.-Y. Yang, G. Qin and M. Hu, *Applied Physics Letters*, 2016, **109**, 242103.
70 G. Qin, Z. Qin, W.-Z. Fang, L.-C. Zhang, S.-Y. Yue, Q.-B. Yan, M. Hu and G. Su, *Nanoscale*, 2016, **8**, 11306–11319.
71 L. Lindsay and D. A. Broido, *Physical Review B*, 2011, **84**, 155421.
72 A. Jain and A. J. McGaughey, *Computational Materials Science*, 2015, **110**, 115–120.
73 L. Lindsay, D. A. Broido and T. L. Reinecke, *Physical review letters*, 2012, **109**, 095901.

74 C. W. Li, J. Hong, A. F. May, D. Bansal, S. Chi, T. Hong, G. Ehlers and O. Delaire, *Nature Physics*, 2015, **11**, 1063–1069.
75 J. Carrete, N. Mingo and S. Curtarolo, *Applied Physics Letters*, 2014, **105**, 101907.
76 L.-C. Zhang, G. Qin, W.-Z. Fang, H.-J. Cui, Q.-R. Zheng, Q.-B. Yan and G. Su, *Scientific reports*, 2016, **6**, 1–9.
77 L. Lindsay, D. A. Broido and T. L. Reinecke, *Physical Review B*, 2013, **87**, 165201.
78 N. Bonini, J. Garg and N. Marzari, *Nano letters*, 2012, **12**, 2673–2678.
79 L. Lindsay, W. Li, J. Carrete, N. Mingo, D. A. Broido and T. L. Reinecke, *Physical Review B*, 2014, **89**, 155426.
80 Q.-X. Pei, Y.-W. Zhang, Z.-D. Sha and V. B. Shenoy, *Journal of Applied Physics*, 2013, **114**, 033526.
81 Y.-Y. Zhang, Q.-X. Pei, J.-W. Jiang, N. Wei and Y.-W. Zhang, *Nanoscale*, 2016, **8**, 483–491.
82 Z.-Y. Ong, Y. Cai, G. Zhang and Y.-W. Zhang, *The Journal of Physical Chemistry C*, 2014, **118**, 25272–25277.
83 G. Qin and M. Hu, *Small*, 2018, **14**, 1702465.
84 C. Lin, X. Zhang and Z. Rao, *Nano Energy*, 2017, **38**, 249–256.
85 L. Lindsay, D. A. Broido and N. Mingo, *Physical Review B*, 2010, **82**, 115427.
86 H. Wang, G. Qin, G. Li, Q. Wang and M. Hu, *Phys. Chem. Chem. Phys.*, 2017, **19**, 12882–12889.
87 A. V. Petrov and E. L. Shtrum, *Soviet Physics-Solid state*, 1962, **4**, 1061–1065.
88 D. T. Morelli, V. Jovovic and J. P. Heremans, *Physical review letters*, 2008, **101**, 035901.
89 E. J. Skoug and D. T. Morelli, *Physical review letters*, 2011, **107**, 235901.
90 M. D. Nielsen, V. Ozolins and J. P. Heremans, *Lone Pair Electrons Minimize Lattice Thermal Conductivity*.
91 J. P. Heremans, *Nature Physics*, 2015, **11**, 990–991.
92 M. K. Jana, K. Pal, U. V. Waghmare and K. Biswas, *Angewandte Chemie*, 2016, **128**, 7923–7927.
93 Y. Xiao, C. Chang, Y. Pei, D. Wu, K. Peng, X. Zhou, S. Gong, J. He, Y. Zhang and Z. Zeng, *Physical Review B*, 2016, **94**, 125203.
94 X. Zhou, W. Feng, S. Guan, B. Fu, W. Su and Y. Yao, *Journal of Materials Research*, 2017, **32**, 2993–3001.
95 G. Qin, Z. Qin, H. Wang and M. Hu, *Nano Energy*, 2018, **50**, 425–430.